Geophysical Research Letters

RESEARCH LETTER
10.1029/2020GL090241

Key Points:
- The relationship between volcanic SAOD and ERF depends on the time after an eruption, the eruption latitude, and eruption season
- Rapid adjustments reduce the volcanic forcing by an average of 20% predominantly due to a positive shortwave cloud adjustment
- We provide a range of global mean volcanic SAOD to global mean ERF conversions dependent on eruption source parameters

Supporting Information:
- Supporting Information S1
- Supporting Information S2

Correspondence to:
L. R. Marshall and A. Schmidt,
lrm49@cam.ac.uk;
anja.schmidt@ch.cam.ac.uk

Citation:
Marshall, L. R., Smith, C. J., Forster, P. M., Aubry, T. J., Andrews, T., & Schmidt, A. (2020). Large variations in volcanic aerosol forcing efficiency due to eruption source parameters and rapid adjustments. *Geophysical Research Letters*, *47*, e2020GL090241. https://doi.org/10.1029/2020GL090241

Received 19 JUN 2020
Accepted 9 SEP 2020
Accepted article online 14 SEP 2020

©2020. The Authors.
This is an open access article under the terms of the Creative Commons Attribution License, which permits use, distribution and reproduction in any medium, provided the original work is properly cited.

Large Variations in Volcanic Aerosol Forcing Efficiency Due to Eruption Source Parameters and Rapid Adjustments

Lauren R. Marshall[1], Christopher J. Smith[2,3], Piers M. Forster[2], Thomas J. Aubry[4], Timothy Andrews[5], and Anja Schmidt[1,4]

[1]Department of Chemistry, University of Cambridge, Cambridge, UK, [2]Priestley International Centre for Climate, University of Leeds, Leeds, UK, [3]International Institute for Applied Systems Analysis (IIASA), Laxenburg, Austria, [4]Department of Geography, University of Cambridge, Cambridge, UK, [5]Met Office Hadley Centre, Exeter, UK

Abstract The relationship between volcanic stratospheric aerosol optical depth (SAOD) and volcanic radiative forcing is key for quantifying volcanic climate impacts. In their Fifth Assessment Report, the Intergovernmental Panel on Climate Change used one scaling factor between volcanic SAOD and volcanic forcing based on climate model simulations of the 1991 Mt. Pinatubo eruption, which may not be appropriate for all eruptions. Using a large ensemble of aerosol-chemistry-climate simulations of eruptions with different sulfur dioxide emissions, latitudes, emission altitudes, and seasons, we find that the effective radiative forcing (ERF) is on average 20% less than the instantaneous radiative forcing, predominantly due to a positive shortwave cloud adjustment. In our model, the volcanic SAOD-ERF relationship is non-unique and varies widely depending on time since an eruption, eruption latitude, and season due to differences in aerosol dispersion and incoming solar radiation. Our revised SAOD-ERF relationships suggest that volcanic forcing has been previously overestimated.

Plain Language Summary Powerful explosive volcanic eruptions inject sulfur gases high into the atmosphere where they form a layer of sulfate aerosol particles that scatter sunlight back into space, decrease the transparency of the atmosphere, and cause surface cooling. The amount of sunlight that is scattered depends on the location of the layer of particles and particle size. We have used a complex climate model to quantify how eruptions of different magnitudes and occurring in different seasons and locations may affect the climate. We find that the relationship between the transparency of the atmosphere and the resulting climatic impact caused by volcanic sulfate aerosol particles depends on the amount of sunlight and the spread of the aerosol and therefore the time since the eruption, the eruption location, and the season. Our simulations also show that the eruptions reduce the cooling effect of clouds, which reduces the overall effectiveness of volcanoes at cooling the Earth's surface.

1. Introduction

Volcanic sulfate aerosol, formed in the stratosphere following the release of sulfur dioxide (SO_2) during explosive volcanic eruptions, scatters incoming shortwave radiation (ISW) and absorbs longwave (LW) radiation, which leads to surface cooling that has defined the natural variability of climate over the last millennium (Myhre et al., 2013; Schurer et al., 2013; Sigl et al., 2015).

Stratospheric aerosol optical depth (SAOD), which is a measure of the opacity of the stratosphere, is a key property used to estimate the radiative forcing of an eruption. The relationship between the two is a measure of how effective the volcanic aerosol is at forcing climate change and can be used to compare volcanic forcing to other climate forcing agents (Hansen et al., 2005). Traditionally, a constant relationship between SAOD and volcanic forcing is assumed; in the Fifth Assessment Report from the Intergovernmental Panel on Climate Change (IPCC AR5, Myhre et al., 2013), a forcing scaling factor of -25 W m^{-2} per unit change of volcanic SAOD is used. This factor was based on simulations of the 1991 eruption of Mt. Pinatubo in the Goddard Institute for Space Studies (GISS) model E (Hansen et al., 2005). Energy balance models and simple climate models (e.g., Haustein et al., 2019; Smith, Forster, et al., 2018), which continue to underpin IPCC calculations of radiative forcing and are used in studies that assess the 1.5°C target of the Paris Agreement (e.g., Smith et al., 2019), remain dependent on such conversions. Furthermore, studies that estimate

forcing from volcanism on geological timescales (e.g., Landwehrs et al., 2020) rely on using scaling factors to convert SAOD to volcanic forcing.

The use of a single scaling factor is problematic for two main reasons. First, the relationship between SAOD and radiative forcing is dependent on several factors such as the cloud cover, surface albedo, and insolation (e.g., Andersson et al., 2015). Consequently, the relationship may be dependent on the eruption latitude, the magnitude of the SO_2 emission, emission altitude, and the eruption season as these parameters dictate the location and amount of aerosol that forms (Marshall et al., 2019; Toohey et al., 2011, 2013) and may differ from that after 1991 Mt. Pinatubo. Second, the relationship between SAOD and volcanic forcing depends on how the radiative forcing is calculated: whether this is the instantaneous radiative forcing (IRF) at the tropopause or top of atmosphere (TOA), a stratospherically adjusted radiative forcing that accounts for changes in stratospheric temperature (e.g., the IPCC AR5 -25 W m^{-2} per unit SAOD value), or the effective radiative forcing (ERF), which accounts for additional radiative effects (termed rapid adjustments [RAs]) due to changes in the surface land temperature, surface albedo, the tropospheric temperature, water vapor, and clouds (Forster et al., 2013; Smith, Kramer, et al., 2018). Studies have found that when RAs are included, the total volcanic radiative forcing for large-magnitude eruptions (i.e., 1991 Mt. Pinatubo magnitude) is around 20% weaker than that used in the IPCC AR5, due to positive aerosol-cloud interactions that reduce the magnitude of the negative radiative forcing (Gregory et al., 2016; Larson & Portmann, 2016; Schmidt et al., 2018). However, these studies are based on relatively few historical eruptions, and a systematic investigation into the effectiveness of volcanic forcing across eruptions of different magnitude and with different source parameters has not been conducted.

2. Methods

2.1. Aerosol-Chemistry-Climate Model Simulations

We have used aerosol-chemistry-climate model simulations of a wide range of eruptions that inject SO_2 into the stratosphere to investigate the relationship between SAOD and the ERF. The ERF is the best indication of the resulting temperature response of a particular forcing agent (Forster et al., 2016; Myhre et al., 2013; Sherwood et al., 2015). Simulations were run using the UM-UKCA interactive stratospheric aerosol model, which includes the HadGEM3-GA4 climate model (Walters et al., 2014), the GLOMAP-mode prognostic aerosol scheme (Mann et al., 2010), and interactive whole-atmosphere chemistry as described in Marshall et al. (2019). Volcanic eruptions are simulated by adding an emission of SO_2 so that changes in aerosol number, mass, and size are accounted for when calculating SAOD. Prescribed SAOD data sets derived from ice-core records of sulfate deposition (Crowley & Unterman, 2013; Gao et al., 2008; Toohey & Sigl, 2017) used in previous modeling studies are uncertain and do not include many microphysical and dynamical effects of the aerosol on the resulting optical properties (Toohey et al., 2016). Our simulations were free-running so that aerosol perturbations can feed back onto the model's dynamics and atmosphere-only with prescribed climatological sea surface temperatures (SSTs) that allow the ERF to be diagnosed (Forster et al., 2016; Smith, Kramer, et al., 2018). ERF is calculated as the difference in the net (shortwave [SW] + LW) all-sky TOA energy imbalance between the simulation with the volcanic SO_2 emission and a control simulation with no eruption (all other aspects of the two model simulations remain the same). Similarly, we examine the change in SAOD at 550 nm between the two simulations (the volcanic SAOD). The calculation of IRF is outlined in section 2.2.

We simulated 82 explosive eruptions with different values of the SO_2 emission, eruption latitude, and the emission height, termed eruption source parameters (ESPs), and with half of the eruptions occurring on the 1 January, and half with the eruption occurring on the 1 July (with the same combinations of the ESPs). The July simulations are presented in Marshall et al. (2019) and were repeated for the 1 January eruption start date. The value of each ESP in each simulation was determined using a Latin Hypercube design as described in Marshall et al. (2019) (see their Figure 1), with SO_2 emissions ranging between 10 and 100 Tg of SO_2, eruption latitude between 80°S and 80°N, and a 3-km-deep emission column ranging between 15–18 km and 25–28 km leading to very good coverage of the three-dimensional parameter space. The SO_2 emissions range from that of 1991 Mt. Pinatubo, estimated to be between 10 and 20 Tg (Guo et al., 2004; Timmreck et al., 2018), to 1815 Mt. Tambora (~60 Tg; Zanchettin et al., 2016) and approaching that of 1257 Samalas (~119 Tg; Toohey & Sigl, 2017). Each simulation was run for 38 months following the

eruption and was initialized during the easterly phase of the Quasi Biennial Oscillation. We do not run additional ensemble members for each eruption but group the eruptions into subsets in which we analyze average responses focusing on annual and global means that have a reasonably low sensitivity to meteorological variability. This is supported by previous UM-UKCA ensemble members of the large-magnitude (~60-Tg SO_2) Mt. Tambora eruption (Marshall et al., 2018; Zanchettin et al., 2016) in which global mean SAOD was very similar.

2.2. Diagnosing IRF and RAs

For each of the 82 eruptions we calculate RAs using the radiative kernel method (Shell et al., 2008; Soden et al., 2008). Differences between simulated responses of surface temperature, atmospheric temperature, specific humidity, and surface albedo are taken from each eruption and its corresponding control (January or July) and multiplied by the radiative kernel based on the HadGEM3-GA7.1 climate model (Smith et al., 2020). The kernel converts a perturbation in atmospheric state to a TOA radiative flux based on the latitude, longitude, height, and month of the perturbation.

For SW cloud RAs we use the Approximate Partial Radiative Perturbation (APRP) technique (Taylor et al., 2007), which approximates the scattering and absorption of SW radiation through the atmosphere by clouds without specialized model diagnostics. LW cloud RAs are estimated by substituting cloud fields from each experiment into the base climatology, and vice versa, running both configurations through the SOCRATES offline radiative transfer code (Edwards & Slingo, 1996; Manners et al., 2015), which is the radiation module used in UM-UKCA, and taking the average of the "forward" and "reverse" substitutions. This offline substitution method is akin to a partial radiative perturbation (Wetherald & Manabe, 1988). The IRF is then estimated as the difference between the ERF and the sum of all RAs (Smith, Kramer, et al., 2018).

3. Results and Discussion

3.1. The Relationship Between Global Annual-Mean Volcanic SAOD and Radiative Forcing

Figure 1 shows a series of different regressions to explore the relationship between volcanic SAOD and volcanic radiative forcing. To compare directly with previous conversions, we show first in Figure 1a the global annual-mean volcanic SAOD regressed against both the IRF and ERF for the 3 years following each eruption across all 82 simulations. The slope of each regression line gives the scaling factor in terms of radiative forcing (IRF or ERF) per unit of SAOD. Across all eruptions the IRF is stronger than the ERF, demonstrating that total RAs are positive, acting to reduce the magnitude of the forcing, in agreement with previous studies (Gregory et al., 2016, 2019; Hansen et al., 2005; Larson & Portmann, 2016; Schmidt et al., 2018). We explore the RAs further in section 3.2. Consequently, the IRF scaling factor is larger than the ERF scaling factor, estimated from the regression slopes as -20.5 ± 0.2 W m^{-2} and -17.0 ± 0.2 W m^{-2}, respectively.

The linear regression fit for IRF over small SAOD values (<0.1, Figure 1a inset: -26.1 ± 0.2 W m^{-2} per unit SAOD) can be directly compared to the IPCC AR5 scaling factor, which is derived from SAOD values also less than ~0.1. Although IPCC AR5 uses the -25 W m^{-2} per unit SAOD factor, additional simulations run with the GISS model E for 1991 Pinatubo using fixed SSTs produce a scaling factor of -26 W m^{-2} per unit SAOD (https://data.giss.nasa.gov/modelforce/strataer/). Because we also use fixed SSTs in our model simulations, we subsequently use the -26 W m^{-2} factor to compare our results to IPCC AR5 (following Schmidt et al., 2018). Our scaling for IRF over small SAOD values is consequently identical to that of IPCC AR5. Our scaling for the ERF and small SAOD values (-18.6 ± 0.3 W m^{-2} per unit SAOD) is smaller than that calculated by Schmidt et al. (2018) using CESM1-WACCM simulations when regressing for the years 1982–1985 and 1991–1994 characterized by the eruptions of El Chichón and Mt. Pinatubo and SAOD also less than ~0.1 (-21.5 ± 1.1 W m^{-2} per unit SAOD; blue line in their Figure 6). This is because we do not include an intercept in our fits so that a zero change in SAOD does not result in a radiative forcing. If we do include an intercept, our scaling factor is -20.9 ± 0.7 W m^{-2} per unit SAOD, which compares very well to Schmidt et al. (2018).

The spread around the regression line in Figure 1a collapses if we account for the spatial distribution of the sulfate aerosol and the ISW. We first transform the globally and temporally resolved SAOD to $1 - e^{-\mathrm{SAOD}}$ (based on a simple application of the Beer-Lambert law) and multiply by the ISW before taking the global

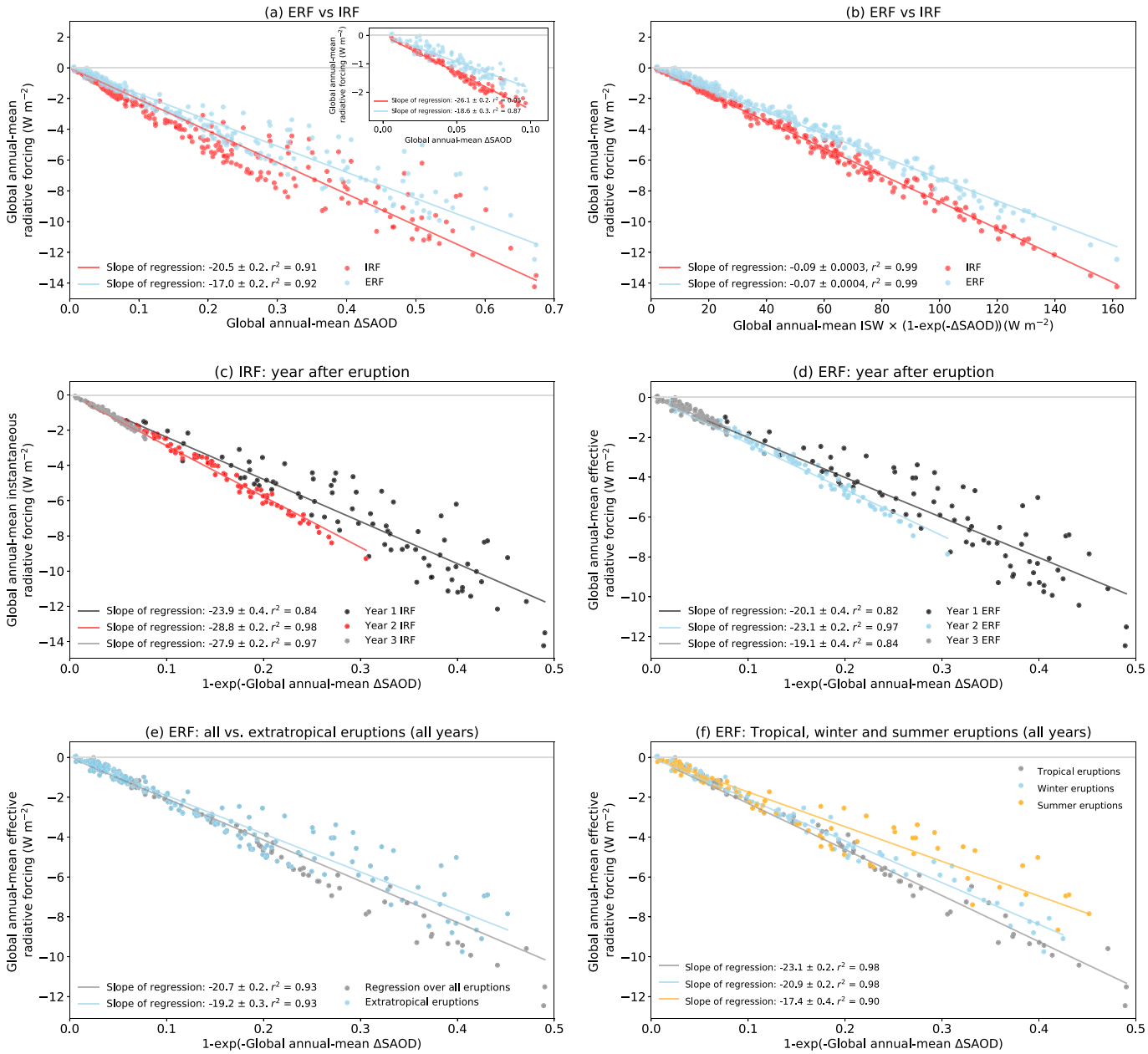

Figure 1. (a) Regression of global annual-mean volcanic SAOD (at 550 nm) against the IRF (red) and ERF (blue) for all 82 simulations. The scatter points show the two quantities in each of the 3 years after each eruption (82 simulations × 3 years giving 246 data points). The inset shows the regression for SAOD values less than 0.1, upon which the IPCC AR5 scaling factor is based. (b) Global annual mean of $1 - e^{-\mathrm{SAOD}}$ multiplied by the incoming shortwave radiation (ISW), against IRF and ERF. (c) $1 - e^{-\mathrm{SAOD}}$ against IRF for each year after the eruption. (d) As (c), but for ERF. (e) As (d), but for all and extratropical eruptions for all years. (f) As (d), but for tropical, winter, and summer eruptions for all years. The IRF is shown in Figure S1.

annual mean (Figure 1b). To explore the driving factors of the reduction in this spread, Figures 1c–1f show the eruptions categorized according to the year after eruption, eruption latitude, and eruption season.

We find that the conversion between SAOD and ERF depends on the time after an eruption, eruption latitude, and eruption season because of differences in the aerosol distribution and the magnitude of the incoming solar radiation that result in differences in the magnitude of the IRF. Forcing per unit of SAOD is weaker in Year 1 than in Years 2 and 3 with most of the spread in the data points arising from Year 1 (Figures 1c and 1d). Forcing per unit of SAOD is stronger for tropical eruptions (between 20°S and 20°N) than extratropical eruptions and stronger for winter eruptions than summer eruptions (Figures 1e and 1f).

In the first year following extratropical eruptions, the aerosol is spatially concentrated in the hemisphere in which it was injected and the IRF depends on the strength of the insolation. This results in a dependency on the eruption season as there is more insolation in the summer hemisphere than the winter hemisphere. Because it takes around 6 months for the aerosol to reach peak burden in our simulations, it is the winter eruptions where more aerosol coincides with high summer insolation resulting in a higher forcing. Zonal mean SAOD and ERF alongside the ISW are shown for each eruption category in Figures S2–S4. In the second year after the eruption, the aerosol has dispersed more widely, driven by large-scale circulation timescales, which results in a higher global mean albedo for the same global mean SAOD, resulting in a larger global mean forcing per unit of SAOD (but both the SAOD and forcing have reduced by Year 2). In addition, depending on the eruption season and latitude, the aerosol may spread to areas with higher ISW, which further enhances the global mean forcing per unit of SAOD. By the third year the aerosol has been largely removed. For tropical eruptions, the aerosol spreads to both hemispheres and is longer-lived as well as coinciding with high tropical insolation resulting in higher SAOD and higher forcing. The dependency on latitude and season is therefore mainly present in the first year after the eruption.

The slope of the regressions in Figures 1c–1f can be used to convert global annual-mean SAOD (in the form of $1 - e^{-\mathrm{SAOD}}$) to ERF depending on ESPs. Transforming SAOD to $1 - e^{-\mathrm{SAOD}}$ removes some of the nonlinearity in the data and is chosen here since it is a physically based quantity that relates to forcing. These conversions are listed in Table S1. Although the global mean conversions cannot explain all the variability discussed above, we provide a parameterization of ERF as a function of global annual-mean SAOD for (a) simplicity, (b) connection to previous studies, (c) use in simple modelling, and (d) because global mean SAOD is what we have good observations and reconstructions of. Importantly, the large range in conversions across the different categories of eruptions illustrates that the SAOD to ERF relationship is non-unique and that the current practice of using a single scaling factor to convert between SAOD and forcing is not appropriate for every eruption.

Using the latest reconstruction of global annual-mean volcanic SAOD for the period 500 BCE to 1900 CE shown in Figure 2a (EVA(2k): Toohey & Sigl, 2017), we have calculated three different volcanic radiative forcing time series (Figure 2b): (a) by multiplying the global annual-mean SAOD time series by the IPCC AR5 factor (-26 W m^{-2}); (b) converting the global annual-mean SAOD using the all-eruption average relationship derived here (Figure 1e), $\mathrm{ERF} = -20.7 \times (1 - e^{-\mathrm{SAOD}})$; and (c) converting the global annual-mean SAOD using our ESP-dependent relationships (Table S1 and Figures 1e and 1f) for tropical, extratropical (if season is unknown), winter, and summer eruptions depending on the latitude and season of each eruption from the reconstruction. In this example, annual SAOD values are calendar years. We do not convert EVA SAOD depending on the year after the eruption as the ESP-dependent relationships account for a large amount of the variability in the SAOD to ERF conversion (Figure 1f) and the temporal evolution in the EVA reconstruction is based on a simple box model with decay timescales that are different to aerosol-climate models that explicitly account for volcanic SO_2 emissions (Aubry et al., 2020; Zanchettin et al., 2016).

The total time-integrated forcing between 500 BCE and 1900 CE using our ESP-dependent conversions is 79% of the total time-integrated forcing when using the IPCC AR5 factor ($-15{,}977$ MJ m^{-2} vs. $-20{,}191$ MJ m^{-2}). When using the all-eruption average conversion, the total time-integrated forcing is only 75% of the IPCC AR5 total ($-15{,}233$ MJ m^{-2}) (Figures 2b and 2c). Consequently, around 20–25% less energy has been lost from the climate system due to volcanic radiative forcing between 500 BCE and 1900 CE than implied by the IPCC AR5.

Figure 2d shows global annual-mean surface temperature anomalies calculated in a simple climate model, FaIR (Finite Amplitude Impulse-Response simple climate-carbon-cycle model) v1.4 (Millar et al., 2017; Smith, Forster, et al., 2018), forced with the three volcanic forcing time series from Figure 2b. No other forcing agents are used such that the temperature response is that from volcanic forcing only. To ensure that the climate is in balance long-term and to avoid a long-term cooling trend, the volcanic forcing input to FaIR in Figure 2b is adjusted such that the mean forcing over the time series is zero (resulting in small positive ERF in volcanically quiescent years). The simulated peak global mean surface cooling differs by up to 0.4–0.5°C for the largest eruptions depending on the conversion used, demonstrating that there are substantial uncertainties on the magnitude of past volcanic climate impacts. For example, using the IPCC AR5 scaling, simulated peak global mean cooling following the 1257 Samalas eruption is -1.5°C (occurring in 1259) and for

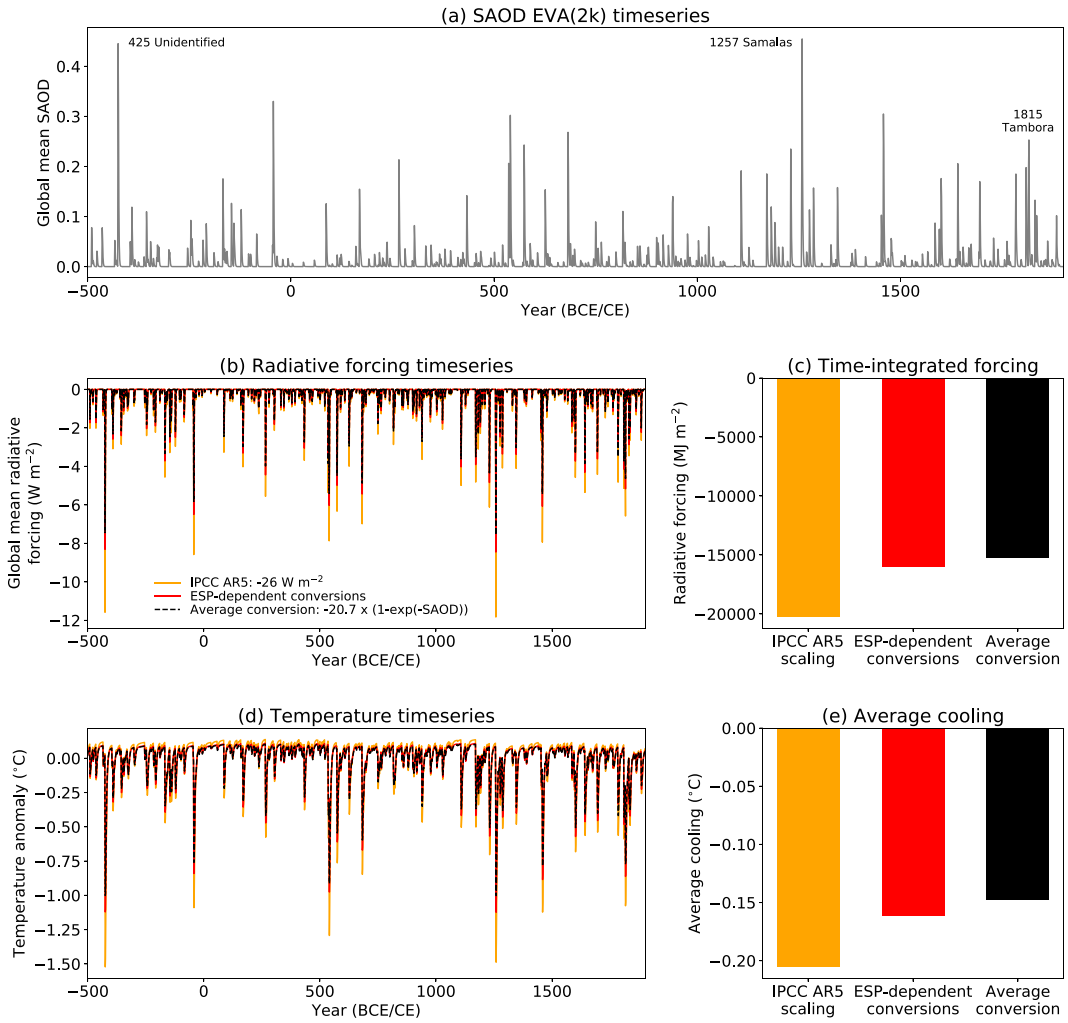

Figure 2. (a) Global annual-mean volcanic SAOD time series from the EVA(2k) reconstruction (calendar years), which does not include background sulfur emissions so that SAOD represents the change due to volcanic eruptions only. (b) Volcanic forcing calculated from the SAOD using the IPCC AR5 scaling factor (orange), eruption source parameter (ESP)-dependent conversions (Table S1) (red), and the all-eruption average conversion (black). (c) Time-integrated forcing from 500 BCE to 1900 CE for the three conversion methods. (d) Global annual-mean surface temperature anomalies (relative to the 2,400-year average from each time series) calculated in a simple climate model (FaIR) for each volcanic forcing time series. (e) The average cooling for temperature anomalies less than 0 for the three conversion methods.

1815 Mt. Tambora is −1.1°C (occurring in 1816). Using the average conversion, the peak cooling is −1.0°C following Samalas and −0.8°C following Tambora. For the ESP-dependent conversions, the peak cooling is −1.1°C for Samalas and −0.9°C for Tambora. These predicted surface temperature changes fall within the range of estimated cooling from proxy reconstructions; tree-ring reconstructions of NH extratropical summer land cooling following 1257 Samalas and 1815 Mt. Tambora eruptions are −0.8°C to −1.3°C (Stoffel et al., 2015). A comparison of the average global mean cooling resulting from applying the different conversions across the whole time series is shown in Figure 2e.

3.2. The Role of RAs

In all simulations, the total global mean RAs integrated over the duration of the simulations are positive, and therefore, the ERF is less than the IRF. Figure 3 shows the normalized time-integrated RAs (divided by the magnitude of the time-integrated IRF so the sign is preserved) averaged over the different subsets of eruptions. On average, the positive RAs reduce the volcanic forcing by 20% and are dominated by a positive SW cloud adjustment (Figure 3g) driven by cloud changes that reduce reflected SW radiation. It is not

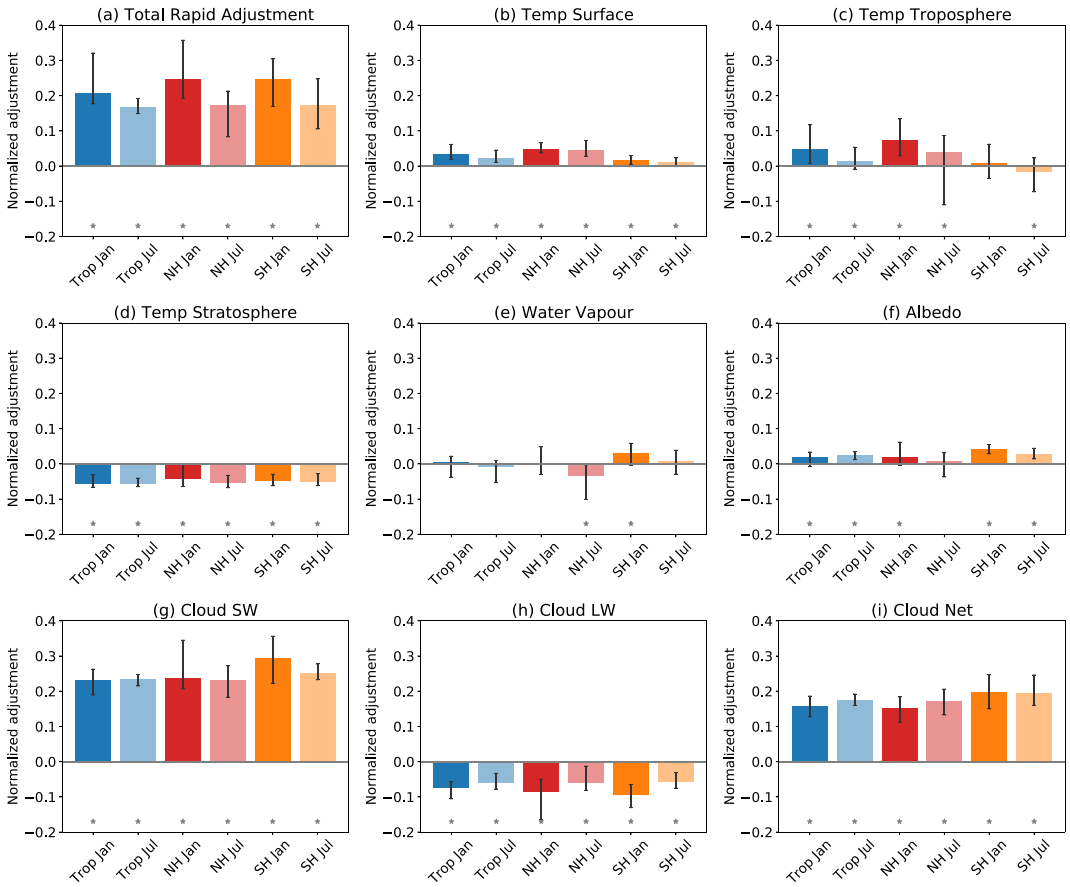

Figure 3. Time-integrated global mean rapid adjustments (a–i) averaged across the different eruption subsets. Rapid adjustments in each simulation were divided by the magnitude of the time-integrated global mean IRF (keeping positive rapid adjustments positive). The total rapid adjustment is shown in Figure 3a, and the remaining subplots show the breakdown of the total rapid adjustment into the contributing components. Error bars show the range in the rapid adjustments among the eruptions in each subset. Stars indicate where the adjustment is significant at the 95% confidence level according to a two-sided Student's *t* test.

possible with our model diagnostics to attribute this adjustment to specific cloud changes, but we do simulate a large reduction in high-level clouds consistent with studies that investigated cloud changes due to sulfate geoengineering (e.g., Krishnamohan et al., 2019; Kuebbeler et al., 2012; Visioni et al., 2018) and some smaller changes to low-level clouds (Figure S5). Our result agrees with that of Gregory et al. (2016) for SW cloud adjustments, who also investigated the radiative forcing from volcanic eruptions. Their study did not diagnose the LW cloud adjustment. We find a small negative LW adjustment from a reduction in cloud fraction (Figure 3h). In contrast, Schmidt et al. (2018) found a positive net aerosol-cloud adjustment following eruptions in CESM1-WACCM due to a positive LW aerosol-cloud interaction. This is further evidence that the sign and magnitude of aerosol-cloud interactions following volcanic eruptions remain highly uncertain and model dependent.

The remainder of the RAs are much smaller, although most are still statistically significant (Student's *t* test; stars in Figure 3). The spatial signatures of the RAs are shown in Figures S6–S11. In general, the surface and tropospheric temperature adjustments are positive (i.e., surface and tropospheric cooling leads to a reduction in outgoing LW radiation), and the stratospheric temperature adjustment is negative (i.e., stratospheric warming following LW absorption by the sulfate aerosols leads to an increase in emissivity). The tropospheric temperature adjustment is strongest for the NH eruptions and weakest for the SH eruptions likely because of the greater proportion of land that can cool in the NH where the forcing occurs. The water vapor adjustment is both positive and negative but is generally not statistically significant except for summer eruptions. The water vapor adjustment reflects a balance between a decrease in tropospheric water vapor due to

cooling and an increase in stratospheric water vapor due to aerosol heating (Dessler et al., 2013; Krishnamohan et al., 2019). The surface albedo adjustment is also positive, reflecting changes in aerosol optical depth, snow cover, and clouds.

The differences in the relationship between SAOD and ERF are predominantly due to the differences in the magnitude of IRF outlined in section 3.1. However, we also find some differences in the normalized total RAs and hence the ERF to IRF ratio, depending on the ESPs, and the time since an eruption. For example, the proportion of the IRF that is offset by the positive RAs is consistently larger for eruptions occurring in January, regardless of the latitude (Figure 3a). For the January eruptions, the RAs are ~23% of the IRF and ~17% of the IRF for the July eruptions. This is mainly driven by the surface and tropospheric temperature adjustments, which are stronger for the January eruptions (Figures 3b and 3c). Spatial plots of the tropospheric temperature adjustment for January eruptions (Figures S6, S8, and S10) show a large positive adjustment near Greenland, suggesting that changes in circulation are driving this adjustment for eruptions in both hemispheres.

The relative role of the total RAs also increases over time (see Figure S12). For January eruptions RA/IRF is 19% in Year 1, 24% in Year 2, and 48% in Year 3, although the forcing and RAs are extremely small and noisy in Year 3 and are therefore less important. The corresponding percentages for July eruptions are 16% (Year 1), 18% (Year 2), and 25% (Year 3). The relative importance of all RAs changes in each year and in opposing directions and depends on the eruption month. The changing RA/IRF ratio is therefore not attributable to a single adjustment and likely changes over time because of different timescales and spatial patterns of the RAs that depend on the spatial and microphysical evolution of the aerosol.

4. Conclusions

The conversion between global mean volcanic SAOD and global mean ERF is an important relationship to understand volcanic climate forcing efficiency and required by simple climate models that continue to underpin IPCC assessments.

Previous studies have focused on a limited number of eruptions to determine the relationship between SAOD and volcanic radiative forcing. We have investigated this relationship across aerosol-climate model simulations of a very wide range of eruptions with different SO_2 emission magnitudes (10–100 Tg of SO_2), latitudes (80°S to 80°N), and for eruptions in January and July. We have shown that the SAOD to ERF relationship is non-unique and varies widely depending on the aerosol distribution and incoming solar radiation and consequently the time after an eruption, eruption season, and eruption latitude. For eruption categories investigated here, forcing per unit of SAOD is weaker in the first year following an eruption than in Years 2 and 3, is stronger for tropical eruptions than extratropical eruptions, and is stronger for winter eruptions than summer eruptions.

We find that the average scaling factor (across all eruption categories) between SAOD and ERF is -17.0 ± 0.2 W m^{-2}, which is considerably lower than the factor of -26 W m^{-2} per unit SAOD used by IPCC AR5. In our study this is because positive RAs dominated by a positive SW cloud adjustment act to reduce the volcanic forcing; the ERF is on average 20% less than the IRF. Total RAs are on average stronger for January eruptions regardless of eruption latitude, offsetting ~23% of the IRF compared to ~17% for the July eruptions due to a larger surface and tropospheric temperature adjustment that occurs for January eruptions. Our results provide evidence that uncertainty in volcanic forcing estimates based on volcanic SAOD and therefore volcanic climatic impacts is large. Our results also suggest that volcanic forcing has been previously overestimated, which has implications for transient energy balance calculations used to constrain the transient climate response and equilibrium climate sensitivity. For example, we find that the time-integrated volcanic ERF for eruptions between 500 BCE and 1900 CE is around 20% less than that based on the IPCC AR5 scaling factor with resulting differences in peak global mean surface cooling following the largest eruptions of up to 0.4°C.

We provide several conversions between global annual-mean volcanic SAOD (in the form of $1 - e^{-\mathrm{SAOD}}$) and ERF (Figure 1 and Table S1). These conversions do not account for all variability we find in the relationship between SAOD and ERF, and which may also vary depending on the model used and atmospheric background state, but provide a considerable improvement on the single scaling factor as used by IPCC AR5.

Data Availability Statement

This work used the ARCHER U.K. National Supercomputing Service (http://www. archer.ac.uk) and JASMIN super-data cluster (doi: 10.1109/BigData.2013.6691556), via the Centre for Environmental Data Analysis (CEDA). Summary model data are available at https://doi.org/10.5285/232164e8b1444978a41f2acf8bbbfe91 and are in the supporting information (Tables S2–S15).

Acknowledgments

We thank Jonathan Gregory for valuable and insightful comments and feedback, which greatly improved this work. We also thank Matthew Toohey for providing the EVA(2k) simulations with no background aerosol included and two anonymous reviewers for their constructive comments that helped improve this paper. L. M. and A. S. are funded by the U.K. Natural Environment Research Council (NERC) via the "Vol-Clim" grant (NE/S000887/1). P. M. F., C. J. S., and T. A. acknowledge support from the European Union's Horizon 2020 Grant Agreement Number 820829 (CONSTRAIN). P. M. F., C. J. S., and A. S. also acknowledge funding from NERC under Project NE/N006038/1 (SMURPHS). C. J. S. was additionally supported by a NERC/IIASA Collaborative Research Fellowship (NE/T009381/1). T. J. A. acknowledges funding from the Royal Society through a Newton International Fellowship (Grant Number NIF\R1\180809) and from the Sidney Sussex College through a Junior Research Fellowship. T. A. was supported by the Met Office Hadley Centre Climate Programme funded by Department for Business, Energy and Industrial Strategy (BEIS) and Department for Environment, Food and Rural Affairs (Defra).

References

Andersson, S. M., Martinsson, B. G., Vernier, J. P., Friberg, J., Brenninkmeijer, C. A. M., Hermann, M., et al. (2015). Significant radiative impact of volcanic aerosol in the lowermost stratosphere. *Nature Communications*, *6*, 7692. https://doi.org/10.1038/ncomms8692

Aubry, T. J., Toohey, M., Marshall, L., Schmidt, A., & Jellinek, A. M. (2020). A new volcanic stratospheric sulfate aerosol forcing emulator (EVA_H): Comparison with interactive stratospheric aerosol models. *Journal of Geophysical Research: Atmospheres*, *125*, e2019JD031303. https://doi.org/10.1029/2019JD031303

Crowley, T., & Unterman, M. B. (2013). Technical details concerning development of a 1200 yr proxy index for global volcanism. *Earth System Science Data*, *5*, 187–197. https://doi.org/10.5194/essd-5-187-2013

Dessler, A. E., Schoeberl, M. R., Wang, T., Davis, S. M., & Rosenlof, K. H. (2013). Stratospheric water vapor feedback. *Proceedings of the National Academy of Sciences*, *110*, 18,087–18,091. https://doi.org/10.1073/pnas.1310344110

Edwards, J. M., & Slingo, A. (1996). Studies with a flexible new radiation code.1. Choosing a configuration for a large-scale model. *Quarterly Journal of the Royal Meteorological Society*, *122*(531), 689–719. https://doi.org/10.1002/qj.49712253107

Forster, P. M., Andrews, T., Good, P., Gregory, J. M., Jackson, L. S., & Zelinka, M. (2013). Evaluating adjusted forcing and model spread for historical and future scenarios in the CMIP5 generation of climate models. *Journal of Geophysical Research: Atmospheres*, *118*, 1139–1150. https://doi.org/10.1002/jgrd.50174

Forster, P. M., Richardson, T., Maycock, A. C., Smith, C. J., Samset, B. H., Myhre, G., et al. (2016). Recommendations for diagnosing effective radiative forcing from climate models for CMIP6. *Journal of Geophysical Research:Atmospheres*, *121*, 12,460–412,475. https://doi.org/10.1002/2016JD025320

Gao, C., Robock, A., & Ammann, C. (2008). Volcanic forcing of climate over the past 1500 years: An improved ice core-based index for climate models. *Journal of Geophysical Research*, *113*, D23111. https://doi.org/10.1029/2008jd010239

Gregory, J. M., Andrews, T., Ceppi, P., Mauritsen, T., & Webb, M. J. (2019). How accurately can the climate sensitivity to CO_2 be estimated from historical climate change? *Climate Dynamics*, *54*, 129–157. https://doi.org/10.1007/s00382-019-04991-y

Gregory, J. M., Andrews, T., Good, P., Mauritsen, T., & Forster, P. M. (2016). Small global-mean cooling due to volcanic radiative forcing. *Climate Dynamics*, *47*, 3979–3991. https://doi.org/10.1007/s00382-016-3055-1

Guo, S., Rose, W. I., Bluth, G. J. S., & Watson, I. M. (2004). Particles in the great Pinatubo volcanic cloud of June 1991: The role of ice. *Geochemistry, Geophysics, Geosystems*, *5*, Q05003. https://doi.org/10.1029/2003gc000655

Hansen, J., Sato, M., Ruedy, R., Nazarenko, L., Lacis, A., Schmidt, G. A., et al. (2005). Efficacy of climate forcings. *Journal of Geophysical Research:Atmospheres*, *110*. Review, D18104. https://doi.org/10.1029/2005jd005776

Haustein, K., Otto, F. E. L., Venema, V., Jacobs, P., Cowtan, K., Hausfather, Z., et al. (2019). A limited role for unforced internal variability in twentieth-century warming. *Journal of Climate*, *32*, 4893–4917. https://doi.org/10.1175/jcli-d-18-0555.1

Krishnamohan, K. P. S. P., Bala, G., Cao, L., Duan, L., & Caldeira, K. (2019). Climate system response to stratospheric sulfate aerosols: Sensitivity to altitude of aerosol layer. *Earth System Dynamics*, *10*, 885–900. https://doi.org/10.5194/esd-10-885-2019

Kuebbeler, M., Lohmann, U., & Feichter, J. (2012). Effects of stratospheric sulfate aerosol geo-engineering on cirrus clouds. *Geophysical Research Letters*, *39*, l23803. https://doi.org/10.1029/2012gl053797

Landwehrs, J. P., Feulner, G., Hofmann, M., & Petri, S. (2020). Climatic fluctuations modeled for carbon and sulfur emissions from end-Triassic volcanism. *Earth and Planetary Science Letters*, *537*, 116174. https://doi.org/10.1016/j.epsl.2020.116174

Larson, E. J. L., & Portmann, R. W. (2016). A temporal kernel method to compute effective radiative forcing in CMIP5 transient simulations. *Journal of Climate*, *29*, 1497–1509. https://doi.org/10.1175/JCLI-D-15-0577.1

Mann, G. W., Carslaw, K. S., Spracklen, D. V., Ridley, D. A., Manktelow, P. T., Chipperfield, M. P., et al. (2010). Description and evaluation of GLOMAP-mode: A modal global aerosol microphysics model for the UKCA composition-climate model. *Geoscientific Model Development*, *3*(2), 519–551. https://doi.org/10.5194/gmd-3-519-2010

Manners, J., Edwards, J. M., Hill, P., & Thelen, J. C. (2015). *SOCRATES (Suite Of Community RAdiative Transfer codes based on Edwards and Slingo) technical guide*. UK: Met Office.

Marshall, L., Johnson, J. S., Mann, G. W., Lee, L., Dhomse, S. S., Regayre, L., et al. (2019). Exploring how eruption source parameters affect volcanic radiative forcing using statistical emulation. *Journal of Geophysical Research: Atmospheres*, *124*, 964–985. https://doi.org/10.1029/2018JD028675

Marshall, L., Schmidt, A., Toohey, M., Carslaw, K. S., Mann, G. W., Sigl, M., et al. (2018). Multi-model comparison of the volcanic sulfate deposition from the 1815 eruption of Mt. Tambora. *Atmospheric Chemistry and Physics*, *18*, 2307–2328. https://doi.org/10.5194/acp-18-2307-2018

Millar, R. J., Nicholls, Z. R., Friedlingstein, P., & Allen, M. R. (2017). A modified impulse-response representation of the global near-surface air temperature and atmospheric concentration response to carbon dioxide emissions. *Atmospheric Chemistry and Physics*, *17*, 7213–7228. https://doi.org/10.5194/acp-17-7213-2017

Myhre, G., Shindell, D., Bréon, F.-M., Collins, W., Fuglestvedt, J., Huang, J., et al. (2013). Anthropogenic and natural radiative forcing. In T. F. Stocker (Eds.), *Climate change 2013: The physical science basis. Contribution of Working Group I to the Fifth Assessment Report of the Intergovernmental Panel on Climate Change* (pp. 659–740). Cambridge, United Kingdom and New York, NY, USA: Cambridge University Press.

Schmidt, A., Mills, M. J., Ghan, S., Gregory, J. M., Allan, R. P., Andrews, T., et al. (2018). Volcanic radiative forcing from 1979 to 2015. *Journal of Geophysical Research: Atmospheres*, *123*, 12,491–12,508. https://doi.org/10.1029/2018jd028776

Schurer, A. P., Hegerl, G. C., Mann, M. E., Tett, S. F. B., & Phipps, S. J. (2013). Separating forced from chaotic climate variability over the past millennium. *Journal of Climate*, *26*, 6954–6973. https://doi.org/10.1175/jcli-d-12-00826.1

Shell, K. M., Kiehl, J. T., & Shields, C. A. (2008). Using the radiative kernel technique to calculate climate feedbacks in NCAR's Community Atmospheric Model. *Journal of Climate*, *21*(10), 2269–2282. https://doi.org/10.1175/2007JCLI2044.1

Sherwood, S. C., Bony, S., Boucher, O., Bretherton, C., Forster, P. M., Gregory, J. M., & Stevens, B. (2015). Adjustments in the forcing-feedback framework for understanding climate change. *Bulletin of the American Meteorological Society*, *96*, 217–228. https://doi.org/10.1175/BAMS-D-13-00167.1

Sigl, M., Winstrup, M., McConnell, J. R., Welten, K. C., Plunkett, G., Ludlow, F., et al. (2015). Timing and climate forcing of volcanic eruptions for the past 2,500 years. *Nature*, *523*, 543–549. https://doi.org/10.1038/nature14565

Smith, C. J., Forster, P. M., Allen, M., Fuglestvedt, J., Millar, R. J., Rogelj, J., & Zickfeld, K. (2019). Current fossil fuel infrastructure does not yet commit us to 1.5 °C warming. *Nature Communications*, *10*, 101. https://doi.org/10.1038/s41467-018-07999-w

Smith, C. J., Forster, P. M., Allen, M., Leach, N., Millar, R. J., Passerello, G. A., & Regayre, L. A. (2018). FAIR v1.3: A simple emissions-based impulse response and carbon cycle model. *Geoscientific Model Development*, *11*, 2273–2297. https://doi.org/10.5194/gmd-11-2273-2018

Smith, C. J., Kramer, R. J., Myhre, G., Forster, P. M., Soden, B. J., Andrews, T., et al. (2018). Understanding rapid adjustments to diverse forcing agents. *Geophysical Research Letters*, *45*, 12,023–12,031. https://doi.org/10.1029/2018GL079826

Smith, C. J., Kramer, R. J., & Sima, A. (2020). The HadGEM3-GA7.1 radiative kernel: The importance of a well-resolved stratosphere. *Earth System Science Data Discussions*, *2020*, 1–16. https://doi.org/10.5194/essd-2019-254

Soden, B. J., Held, I. M., Colman, R., Shell, K. M., Kiehl, J. T., & Shields, C. A. (2008). Quantifying climate feedbacks using radiative kernels. *Journal of Climate*, *21*(14), 3504–3520. https://doi.org/10.1175/2007JCLI2110.1

Stoffel, M., Khodri, M., Corona, C., Guillet, S., Poulain, V., Bekki, S., et al. (2015). Estimates of volcanic-induced cooling in the Northern Hemisphere over the past 1,500 years. *Nature Geoscience*, *8*, 784–788. https://doi.org/10.1038/ngeo2526

Taylor, K. E., Crucifix, M., Braconnot, P., Hewitt, C. D., Doutriaux, C., Broccoli, A. J., et al. (2007). Estimating shortwave radiative forcing and response in climate models. *Journal of Climate*, *20*(11), 2530–2543. https://doi.org/10.1175/JCLI4143.1

Timmreck, C., Mann, G. W., Aquila, V., Hommel, R., Lee, L. A., Schmidt, A., et al. (2018). The Interactive Stratospheric Aerosol Model Intercomparison Project (ISA-MIP): Motivation and experimental design. *Geoscientific Model Development*, *11*, 2581–2608. https://doi.org/10.5194/gmd-11-2581-2018

Toohey, M., Kruger, K., Niemeier, U., & Timmreck, C. (2011). The influence of eruption season on the global aerosol evolution and radiative impact of tropical volcanic eruptions. *Atmospheric Chemistry and Physics*, *11*(23), 12,351–12,367. https://doi.org/10.5194/acp-11-12351-2011

Toohey, M., Kruger, K., & Timmreck, C. (2013). Volcanic sulfate deposition to Greenland and Antarctica: A modeling sensitivity study. *Journal of Geophysical Research: Atmospheres*, *118*, 4788–4800. https://doi.org/10.1002/jgrd.50428

Toohey, M., & Sigl, M. (2017). Volcanic stratospheric sulfur injections and aerosol optical depth from 500 BCE to 1900 CE. *Earth System Science Data*, *9*, 809–831. https://doi.org/10.5194/essd-9-809-2017

Toohey, M., Stevens, B., Schmidt, H., & Timmreck, C. (2016). Easy Volcanic Aerosol (EVA v1.0): An idealized forcing generator for climate simulations. *Geoscientific Model Development*, *9*, 4049–4070. https://doi.org/10.5194/gmd-9-4049-2016

Visioni, D., Pitari, G., di Genova, G., Tilmes, S., & Cionni, I. (2018). Upper tropospheric ice sensitivity to sulfate geoengineering. *Atmospheric Chemistry and Physics*, *18*, 14,867–14,887. https://doi.org/10.5194/acp-18-14867-2018

Walters, D. N., Williams, K. D., Boutle, I. A., Bushell, A. C., Edwards, J. M., Field, P. R., et al. (2014). The Met Office Unified Model global atmosphere 4.0 and JULES global land 4.0 configurations. *Geoscientific Model Development*, *7*, 361–386. https://doi.org/10.5194/gmd-7-361-2014

Wetherald, R. T., & Manabe, S. (1988). Cloud feedback processes in a general circulation model. *Journal of the Atmospheric Sciences*, *45*(8), 1397–1416. https://doi.org/10.1175/1520-0469(1988)045<1397:CFPIAG>2.0.CO;2

Zanchettin, D., Khodri, M., Timmreck, C., Toohey, M., Schmidt, A., Gerber, E. P., et al. (2016). The Model Intercomparison Project on the climatic response to Volcanic forcing (VolMIP): Experimental design and forcing input data for CMIP6. *Geoscientific Model Development*, *9*, 2701–2719. https://doi.org/10.5194/gmd-9-2701-2016